

Article

Effect of a Substrate's Preheating Temperature on the Microstructure and Properties of Ni-Based Alloy Coatings

Yu Liu ^{1,2}, Haiquan Jin ¹, Tianhao Xu ¹, Zhiqiang Xu ^{1,3}, Fengming Du ⁴, Miao Yu ⁵, Yali Gao ^{1,*}  and Dongdong Zhang ¹

¹ School of Mechanical Engineering, Northeast Electric Power University, Jilin 132012, China

² International Shipping Research Institute, Gongqing Institute of Science and Technology, Gongqing City 332020, China

³ Beijing Electric Power Transmission and Transformation Company Limited, Beijing 102400, China

⁴ Marine Engineering College, Dalian Maritime University, Dalian 116026, China

⁵ Graduate School, Daejin University, Pocheon-si 11159, Republic of Korea

* Correspondence: dehuigyl@126.com

Abstract: Laser cladding is a new technology to fabricate a coating on the surface of a metal substrate. The properties on copper substrates are usually not very good due to the high thermal conductivity and reflectivity. The appropriate preheating temperature is helpful to fabricate coatings with good quality and properties, especially for copper substrates. In order to investigate the effect of different preheating temperatures, four coatings with different preheating temperatures (100, 200, 300 and 400 °C) were fabricated via a laser on a copper substrate. The microstructures and properties of four coatings were investigated using SEM, XRD, EDS, a Vickers microhardness meter, a wear tester and an electrochemical workstation. The results show that the elements from Ni-based alloy powder were uniformly distributed among the binding region, which obtained a good metallurgical bonding. The microstructure was mainly composed of cellular, dendrite and plane crystals, and the main reinforced phases were γ (Fe, Ni), $\text{Cr}_{0.09}\text{Fe}_{0.7}\text{Ni}_{0.21}$, WC and Ni_3B . The values of average microhardness of the four coatings were 614.3, 941.6, 668.1 and 663.1 $\text{HV}_{0.5}$, respectively. The wear rates of the four coatings were $9.7, 4.9, 12.5$ and $13.3 \times 10^{-5} \text{ mm}^3 \cdot \text{N}^{-1} \cdot \text{m}^{-1}$, respectively, which were less than that of the copper substrate ($4.3 \times 10^{-3} \text{ mm}^3 \cdot \text{N}^{-1} \cdot \text{m}^{-1}$). The decrease in wear rate was due to the existence of the reinforced phases, such as WC, Ni_3B , M_7C_3 (M=Fe, Cr) and $\text{Cr}_{0.09}\text{Fe}_{0.7}\text{Ni}_{0.21}$. The fine crystals in the coating preheated at 200 °C also improved the wear resistance. Additionally, the minimum values of corrosion current density were $3.26 \times 10^{-5}, 2.34 \times 10^{-7}, 4.02 \times 10^{-6}$ and $4.21 \times 10^{-6} \text{ mA} \cdot \text{mm}^{-2}$, respectively. It can be seen that the coating preheated at 200 °C had higher microhardness, lower wear rates and better corrosion resistance due to the existence of reinforced phases and fine and uniform crystals.

Keywords: laser cladding; Ni-based alloy; preheating temperature; friction and wear; electrochemistry



Citation: Liu, Y.; Jin, H.; Xu, T.; Xu, Z.; Du, F.; Yu, M.; Gao, Y.; Zhang, D. Effect of a Substrate's Preheating Temperature on the Microstructure and Properties of Ni-Based Alloy Coatings. *Lubricants* **2024**, *12*, 21. <https://doi.org/10.3390/lubricants12010021>

Received: 3 November 2023

Revised: 18 December 2023

Accepted: 19 December 2023

Published: 10 January 2024



Copyright: © 2024 by the authors. Licensee MDPI, Basel, Switzerland. This article is an open access article distributed under the terms and conditions of the Creative Commons Attribution (CC BY) license (<https://creativecommons.org/licenses/by/4.0/>).

1. Introduction

Copper alloys are widely used in the manufacture of condenser tubes for ocean platforms due to their good corrosion resistance [1–3]. However, corrosion failure often occurs during long-term service, which reduces the service life of the condenser tube [4]. In order to improve the corrosion resistance of condenser tubes, some surface modification technologies are used to fabricate coatings, such as electroplating and thermal spraying [5–7].

In recent decades, laser cladding has been widely used to fabricate coatings due to its advantages of high efficiency and low cost [8–12]. As a coating material, a single metal powder or alloy powder plays an indispensable role in laser cladding technology [13,14]. During the process of laser cladding, some self-fluxing powders, such as Fe-based, Ni-based and Co-based ones and high-entropy alloys, are widely used [15–20]. Of these, Ni-based powder is the most widely used during the process of laser cladding because

of its good wear resistance, good corrosion resistance and moderate price [21]. Many researchers have prepared coatings on the surface of copper alloys via laser cladding technology. Bysakh et al. [22] used a CO₂ laser to obtain a cladding layer of a Cu-Fe-Al-Si alloy on the surface of a copper alloy; however, this coating had some defects. Li et al. [23] prepared a Ni60 alloy coating on the surface of aluminum bronze via supersonic flame spraying and then performed laser remelting at a laser power of 3.2 kW with a CO₂ laser. Although a cladding layer with good metallurgical bonding to the substrate was obtained, bubbles still appeared due to the molten pool disturbance. There are many factors affecting the quality of laser cladding, including the laser power, scanning speed, powder feeding rate and preheating temperature [24–27]. In addition, the preheating temperature is one of the key factors of laser cladding that has been studied by many scholars [28–31]. Although the preheating temperatures of different substrates have been studied, there are few studies about the preheating temperature of copper substrate. Because of the higher thermal conductivity and reflectivity of copper substrate, the selection of the preheating temperature is particularly important to fabricate a good coating using a laser.

In this paper, four different preheating temperatures (100, 200, 300 and 400 °C) were selected to fabricate a coating on a copper substrate. The macroscopic morphology and dilution rate were studied. The phases, microstructure, elemental distribution and properties of the four coatings were investigated using SEM, XRD, EDS, a Vickers microhardness meter, a wear tester and an electrochemical workstation. Meanwhile, the microstructure evolution of the four coatings is discussed.

2. Experimental Conditions

2.1. Materials

Copper alloy is used as the substrate; its size is 50 × 30 × 10 mm and its composition is shown in Table 1. Ni-based alloy powder is used as the cladding material; its composition is shown in Table 2. The mass fractions of the Fe, Cr and WC elements are 12.0%, 12.0% and 5.0%, respectively. There are small amounts of the C, B and Si elements.

Table 1. Chemical composition of the copper alloy (wt.%).

Zn	Al	Mn	Fe	Cu
29.0	6.3	3.2	1.4	60.1

Table 2. Chemical composition of the Ni-based alloy powder (wt.%).

Fe	C	B	Si	Cr	WC	Ni
12	1	2.5	1.5	12	5	Bal.

Figure 1 is an SEM micrograph of the Ni-based alloy powder. It can be seen that the shape of most particles is nearly spherical and the surface is smooth. There are a few irregular particles with the shapes resembling a block or strip. Additionally, some particles with small sizes have tended to gather together.

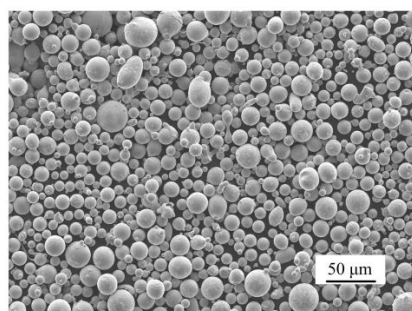


Figure 1. SEM micrograph of the Ni-based alloy powder.

2.2. Methods

The device was a CO₂ laser with a continuous mode and the parameters are as follows: laser power 1.4 kW, laser beam diameter 3.0 mm, scanning speed 2 mm/s and overlapping ratio 30%. The substrate preheating temperatures were 100, 200, 300 and 400 °C, respectively. After laser cladding, the coatings were cut into 10 × 10 × 10 mm samples. After the samples were buffed and polished, a ferric chloride solution was used to etch the cladding coating for 10 s. Then, the samples were observed using optical microscopy and scanning electron microscopy (TESCAN MIRA). At the same time, the element distribution was analyzed via EDS. The phases were detected by X-ray diffraction (TD-3500). The microhardness was tested using a Vickers microhardness meter with a load of 50 gf at 15 s. The microhardness was measured from the top of the Ni-based coating to the copper substrate and each point was repeated five times at the same height. The friction and wear properties were tested using a reciprocating fatigue friction and wear tester (MGW-02) with a tip force of 10 N and a friction frequency 2 Hz. An experiment testing the electrochemical corrosion was also carried out to investigate the corrosion resistance of cladding coatings. A 3.5% NaCl solution was used as the electrolyte in a CHI600E electrochemical workstation.

3. Results

3.1. Macroscopic Morphology and Dilution Rate

Figure 2 shows the macroscopic morphology of coatings preheated at four temperatures (100, 200, 300 and 400 °C). The four coatings can be successively fabricated on copper substrate but there are some pores and cracks on the surface.

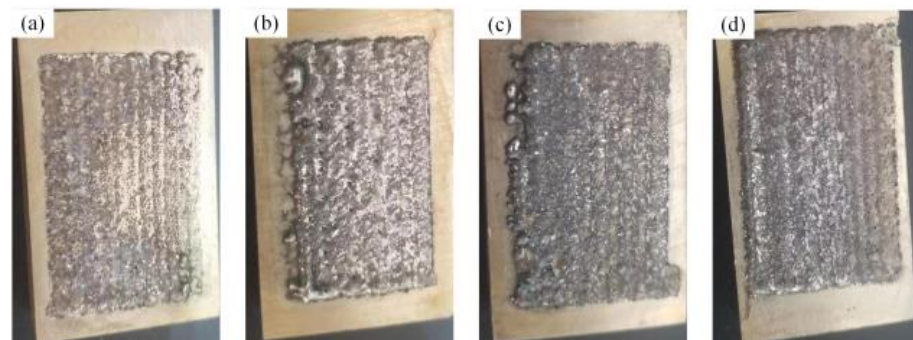


Figure 2. Macroscopic morphology of coatings preheated at four temperatures. (a) 100 °C; (b) 200 °C; (c) 300 °C; (d) 400 °C.

The dilution rate is an important index to judge the performance of a coating. A low dilution rate is helpful to improve the coating's properties. The molten pool depth and height of the coating are two parameters to measure dilution rate, as shown in Figure 3. The dilution rate can be calculated using Equation (1).

$$\eta = \frac{Depth}{Depth + Height} \times 100\% \quad (1)$$

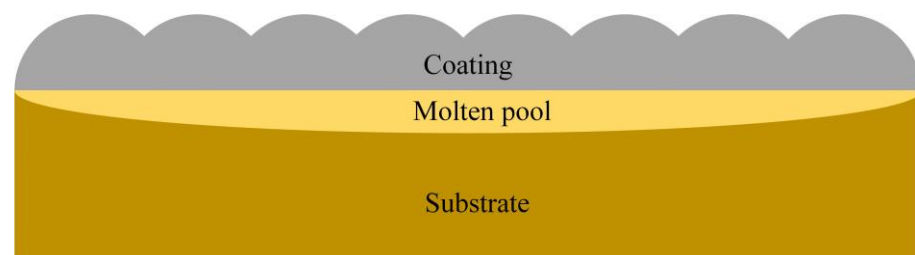


Figure 3. Schematic diagram of the molten pool and coating.

In Equation (1), η is the dilution rate, $Depth$ is the average depth of the coating's molten pool, and $Height$ is the average height of the coating.

Table 3 shows the height, molten pool depth and dilution rate of the four coatings with different preheating temperatures (100, 200, 300 and 400 °C). At the four different preheating temperatures, the coatings' heights are 0.27, 0.48, 0.39 and 0.27 mm, respectively. The depths of the molten pool are 0.1, 0.12, 0.16 and 0.18 mm, respectively. With the increasing preheating temperature, the coatings' heights first increase and then decrease. However, the depths of the molten pool increase gradually along with the increase in the preheating temperature. The main reason for this is that higher preheating temperatures make the substrate easier to melt and so it forms a molten pool with higher temperatures, which increases the depths of the molten pool. At the four different preheating temperatures, the dilution rates were 27%, 20%, 29% and 40%, respectively. The coating with a preheating temperature of 200 °C has the lowest dilution rate (20%), which suggests that it can maintain the properties of the coating and reduce the mixing of elements between the substrate and coating.

Table 3. Heights, molten pool depths and dilution rates of the four coatings.

Preheating Tem. (°C)	100	200	300	400
Height (mm)	0.27	0.48	0.39	0.27
Depth (mm)	0.1	0.12	0.16	0.18
Dilution rate (%)	27	20	29	40

3.2. Phases

The X-ray diffraction patterns of the coatings preheated at four different temperatures (100, 200, 300 and 400 °C) are shown in Figure 4. When the preheating temperature was 100 °C, the main phases are γ (Fe, Ni), WC, W_2C , Ni_3B , and M_7C_3 ($M=Fe, Cr$). When the preheating temperature was 200 °C, the higher preheating temperature increases the heat of the molten pool and prolongs the solidification time of the molten pool. Elements such as Ni, Cr and Fe have enough time to form a reinforced phase. Therefore, a new phase, $Cr_{0.09}Fe_{0.7}Ni_{0.21}$, appears. When the preheating temperatures are 300 and 400 °C, the amount of some elements decreases gradually due to the higher temperature of molten pool, which results in the decrease in WC, W_2C and boride. At the same time, a large number of substrate elements enter into the coating and form $Cu_{0.64}Zn_{0.36}$ and Ni_2W_4C phases.

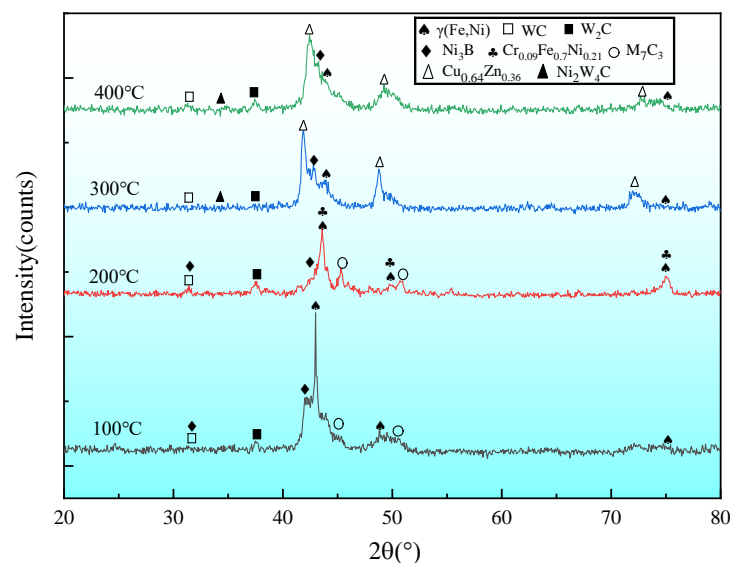


Figure 4. XRD patterns of coatings preheated at four preheating temperatures (100, 200, 300 and 400 °C).

3.3. Microstructure

Figure 5 depicts the microstructures of coatings preheated at four temperatures (100, 200, 300 and 400 °C). Figure 5(a1,b1,c1,d1) shows the microstructure of the coatings' top regions. When the preheating temperature was 100 °C, there are a large number of equiaxed crystals. When the preheating temperatures were 200, 300 or 400 °C, some cellular crystals appear in the top regions. In addition, the coating preheated at 200 °C has fine cellular crystals. As shown in Figure 5(a2,b2,c2,d2), the microstructure of the middle position is mainly a dendrite structure. In addition, when the preheating temperature was 200 °C, the dendrite crystals are fine and uniform. With the increase in preheating temperature, the secondary dendrites grow gradually on the primary dendrites, as shown in Figure 5(c2). When the preheating temperature was 400 °C, the dendrite crystals become larger. At the bottom of the four coatings, when the preheating temperature was 100 °C, some small holes appear in the bonding region, as shown in Figure 5(a3), which decreases the binding strength between the coating and the substrate. With the increase in preheating temperature, the holes gradually disappear, as shown in Figure 5(b3,c3,d3).

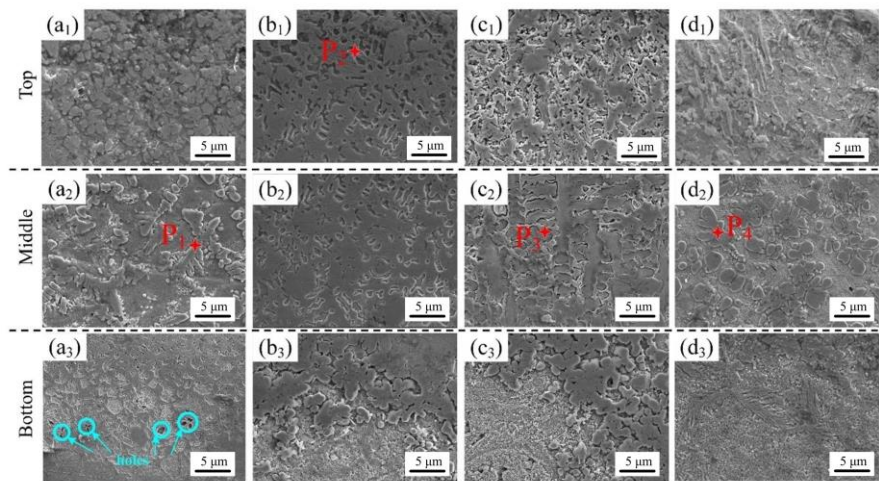


Figure 5. SEM micrographs of four coatings that were preheated at 100 (a1–a3), 200 (b1–b3), 300 (c1–c3) and 400 °C (d1–d3).

Table 4 shows the percentage of element atoms at the P1–P4 points in the four coatings with different preheating temperatures (100, 200, 300 and 400 °C). According to the percentage of element atoms at the P1 point, there are large amounts of Fe and Ni in the coating with the preheating temperature of 100 °C that form the supersaturated solid solution of the γ (Fe, Ni) phase. Some C atoms form WC and W_2C and others form the Fe_7C_3 phase. Compared with the P1 point, the percentage of element atoms at the P2 point shows that the content of Cr increases, which becomes Cr_7C_3 phase. At the same time, there are a few borides. The percentage of element atoms at the P3 and P4 points indicates that a large number of Cu and Zn elements appear at P3 and P4, which is mainly the $Cu_{0.64}Zn_{0.36}$ phase. With the increase in preheating temperature, more and more elements from the substrate enter into the molten pool. This is consistent with the results of Figure 4.

Table 4. Percentage of element atoms at the P1–P4 points in the coatings.

Point	Atomic Concentration %							
	Ni	Fe	C	W	B	Cu	Zn	Cr
P1	25.4	29.6	23.8	9.4	4.5	7.2	-	0.1
P2	39.7	11.6	35.4	5.4	2.8	1.7	-	3.4
P3	31.1	15.2	20.9	3.3	-	16.8	8.8	3.9
P4	25.5	15.4	9.8	5.4	-	23.7	18.6	1.6

Figure 6 depicts the SEM micrograph and EDS element line scanning results for the four coatings with different preheating temperatures (100, 200, 300 and 400 °C). From the substrate to the coating, the copper element decreases gradually, whereas the Ni element increases gradually. In the diffusion zone, Cu and Ni dissolve each other and form good metallurgical bonding. At the same time, the width of the diffusion zone increases with the increase in preheating temperature. When the preheating temperature was 200 °C, the coating has the least amount of Cu. More of the Cu element appears in the diffusion zone, which also decreases the relative amount of the Ni element. The other elements in the substrate and coating, such as Fe, Al and Cr, also enter into the diffusion zone. When the preheating temperature is higher, more of the Cu element enters into the coating, as shown in Figure 6c,d.

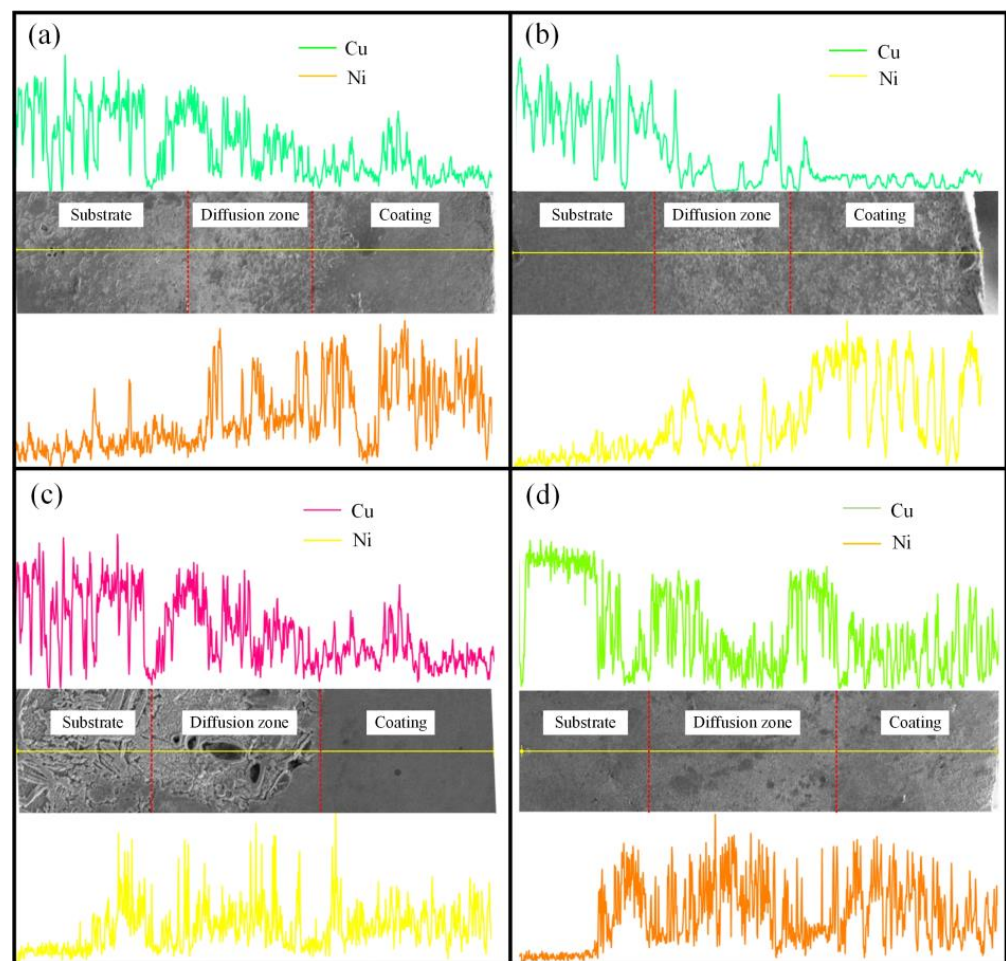


Figure 6. SEM micrograph and EDS line scan results for the four coatings with different preheating temperatures (100, 200, 300 and 400 °C). (a) 100 °C; (b) 200 °C; (c) 300 °C; (d) 400 °C.

3.4. Microhardness

Figure 7 shows the microhardnesses of the four coatings' cross sections. The maximum microhardness values of four the coatings are 680.7, 1069.3, 815.2 and 760.9 HV_{0.5}, respectively. The values for the average microhardness are 614.3, 941.6, 668.1 and 663.1 HV_{0.5}, respectively. As a whole, the microhardness in the strengthening layer is stable and the fluctuation is not very large. At the binding region, the microhardness decreases quickly. When the preheating temperature was 200 °C, the coating has the highest average microhardness (941.6 HV_{0.5}), which is caused by the reinforced phases M₇C₃, WC, Ni₃B and Cr_{0.09}Fe_{0.7}Ni_{0.21} and the fine crystals in the top region. However, when the preheating tem-

perature was 300 °C, some new phases, $\text{Cu}_{0.64}\text{Zn}_{0.36}$ and $\text{Ni}_2\text{W}_4\text{C}$, appear due to entrance of Cu and Zn elements from copper substrate, which decreases the coating's microhardness.

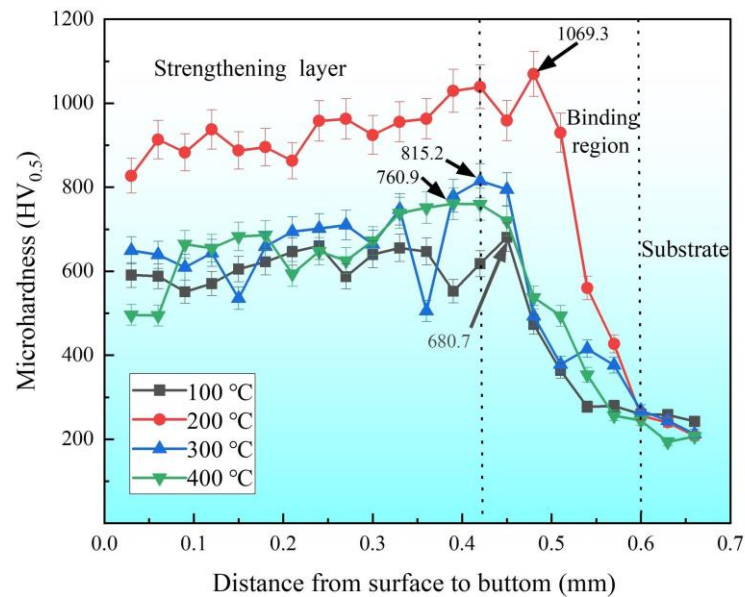


Figure 7. Microhardness of the four coatings' cross sections.

3.5. Wear Resistance

The friction coefficients of four coatings with different preheating temperatures (100, 200, 300 and 400 °C) are shown in Figure 8. The coating that had a preheating temperature of 200 °C has the smallest friction coefficient (around 0.1), which only has a small fluctuation, whereas the coating that had a preheating temperature 400 °C has the largest friction coefficient (around 0.3) and fluctuation. The friction coefficients of the coatings preheated at 100 and 300 °C fluctuate around 0.2 and also have large fluctuations. From the above analysis, the smallest friction coefficient (around 0.1) in the 200 °C preheated coating may be due to its lower surface roughness and fine crystals.

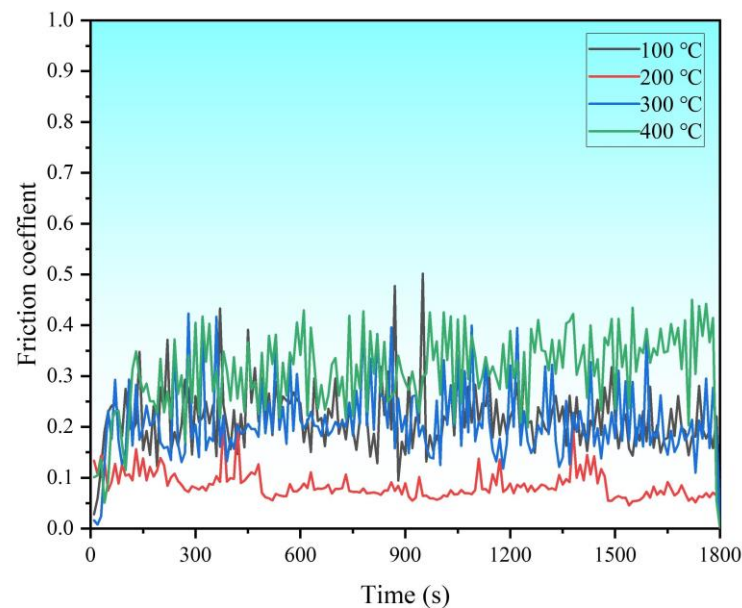


Figure 8. Friction coefficients of coatings preheated at four preheating temperatures (100, 200, 300 and 400 °C).

Figure 9 shows the wear rates of coatings preheated at different temperatures (100, 200, 300 and 400 °C). The wear rates of coatings preheated at 100, 200, 300 and 400 °C are 9.7 , 4.9 , 12.5 and $13.3 \times 10^{-5} \text{ mm}^3 \cdot \text{N}^{-1} \cdot \text{m}^{-1}$, respectively. The wear rate of the coating preheated at 200 °C is the lowest, only about one-third of the wear rate of the coating preheated at 400 °C. The wear rate of copper substrate is $4.3 \times 10^{-3} \text{ mm}^3 \cdot \text{N}^{-1} \cdot \text{m}^{-1}$. Compared with the substrate, the wear resistance of the four coatings has an obvious improvement due to the existence of the reinforced phases, such as WC, Ni₃B, M₇C₃ (M=Fe, Cr) and Cr_{0.09}Fe_{0.7}Ni_{0.21}. Additionally, when the preheating temperature was 200 °C, the coating has more fine crystals in the top region.

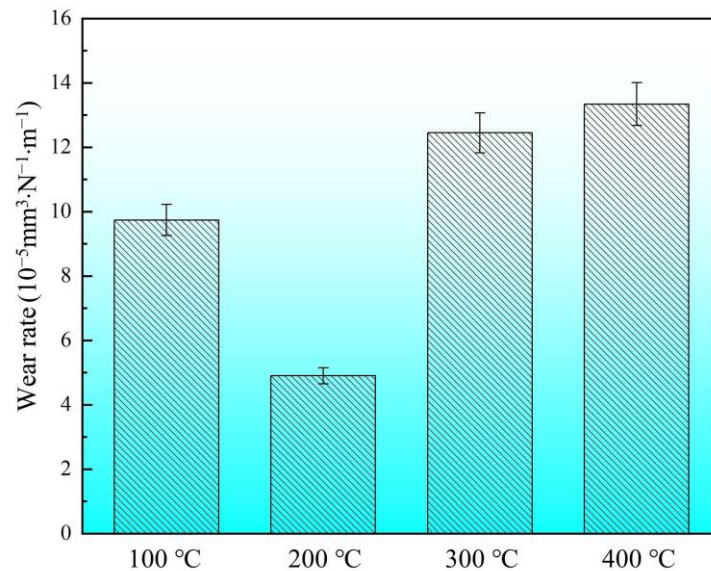


Figure 9. Wear rates of coatings preheated at four preheating temperatures (100, 200, 300 and 400 °C).

Figure 10 depicts the morphology of the friction and wear of coatings preheated at different temperatures (100, 200, 300 and 400 °C). It can be seen that the coating that had a preheating temperature 200 °C has the smallest depth and width of grinding crack. More M₇C₃, WC, W₂C and borides improve the coating hardness and reinforced phase content. Meanwhile, the fine and uniform crystals are also helpful to enhance the wear resistance, which forms abrasive wear and makes the wear volume decrease.

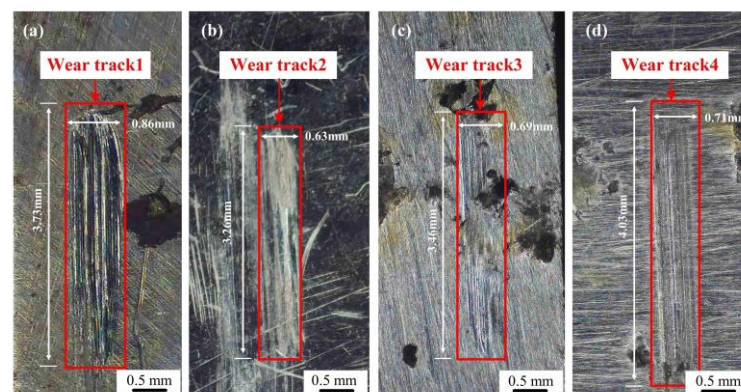


Figure 10. Morphology of friction and wear of coatings preheated at four preheating temperatures (100, 200, 300 and 400 °C). (a) 100 °C; (b) 200 °C; (c) 300 °C; (d) 400 °C.

3.6. Corrosion Resistance

Figure 11 shows the polarization curves of coatings preheated at four temperatures (100, 200, 300 and 400 °C). The polarization curves of the four coatings present a similar trend and show the certain passivation behavior. When the preheating temperatures were

100, 200, 300 and 400 °C, the free corrosion potentials are -0.708 , -0.690 , -0.893 and -0.817 V, respectively. The minimum values of corrosion current density are 3.26×10^{-5} , 2.34×10^{-7} , 4.02×10^{-6} and 4.21×10^{-6} mA·mm⁻², respectively. Moreover, the corrosion current density of the copper substrate is 1.14×10^{-6} mA·mm⁻², which is less than that of the coatings preheated at 100, 300 or 400 °C and more than that of the coating preheated at 200 °C. Therefore, the coating preheated at 200 °C has the lowest corrosion current density (2.34×10^{-7} mA·mm⁻²), which indicates that the coating has the best corrosion resistance due to a large amount of Cr₇C₃. This phase improves the corrosion resistance. Although the coatings with preheating temperatures of 300 and 400 °C have a Cr₇C₃ phase, a lot of Cu and Zn elements diffuse into the coating and reduce the corrosion resistance.

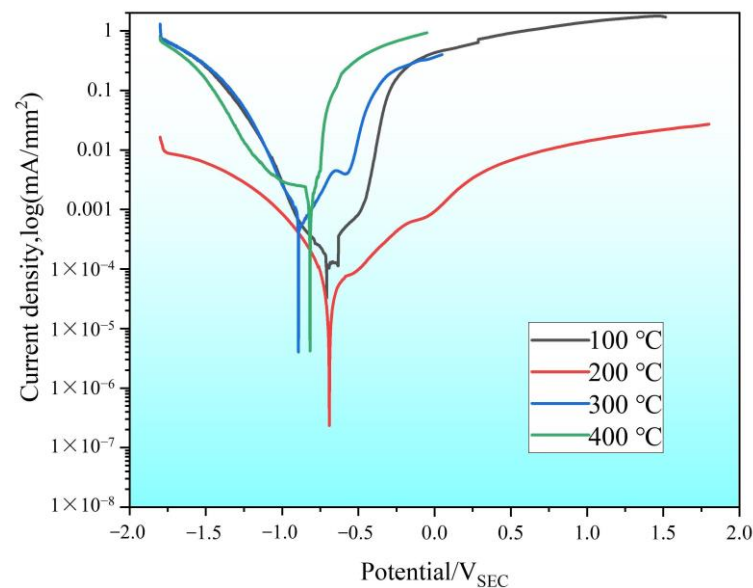


Figure 11. Polarization curves of coatings preheated at four preheating temperatures (100, 200, 300 and 400 °C).

4. Discussion

Ni-based alloy coatings with different preheating temperatures (100, 200, 300 and 400 °C) were fabricated on copper substrate. Due to the difference in preheating temperature, the microstructure, quality and properties of the coatings are different. Therefore, the phases, microstructure, microhardness, wear resistance and corrosion resistance were investigated. The microhardnesses of the coatings were 614.3, 941.6, 668.1 and 663.1 HV_{0.5} under preheating at temperatures of 100, 200, 300 and 400 °C, respectively. The average hardness is highest at the preheating temperature of 200 °C, which is caused by the reinforcing phases such as M₇C₃, WC, Ni₃B and Cr_{0.09}Fe_{0.7}Ni_{0.21} and the diffusion of fine grains and fewer Cu and Zn elements in the top region. The wear rates of the four coatings were 9.7, 225, 4.9, 12.5 and 13.3×10^{-5} mm³·N⁻¹·m⁻¹, respectively. The 200 °C preheated coating has the lowest wear rate, which is due to the correct preheating temperature to produce finer and more uniform crystals in the top area of the coating. In the electrochemical test, the coating preheated at 200 °C has the lowest corrosion current density (2.34×10^{-7} mA·mm⁻²), which is due to the fact that the coating is less affected by the diffusion of Cu and Zn elements and the presence of a large amount of Cr₇C₃ in the coating, resulting in the best corrosion resistance.

4.1. Effect of Preheating Temperature on Pore and Crack

During the laser cladding process, if the gas in molten pool does not escape in time, some pores will appear in the coating. The existence of pores will reduce the mechanical and corrosion resistance of a coating. According to the Stocks equation [32], the gas overflow in the molten pool is mainly related to the viscosity of the liquid metal. With an increase in

temperature, the viscosity of the liquid metal decreases and the gas can more easily escape from the molten pool. Figure 12 shows the schematic diagram of gas overflow in the molten pool during the laser cladding process. At lower preheating temperature, the viscosity is larger, which makes it difficult for the gas to escape and results in some pores being left in the coating, as shown in Figure 12a. This is in accordance with the result shown in Figure 5(a3). In contrast, if the preheating temperature is higher, the gas can more easily escape, as shown in Figure 12b,c. Therefore, no pores appeared in the cladding coating when the preheating temperatures were 200, 300 and 400 °C.

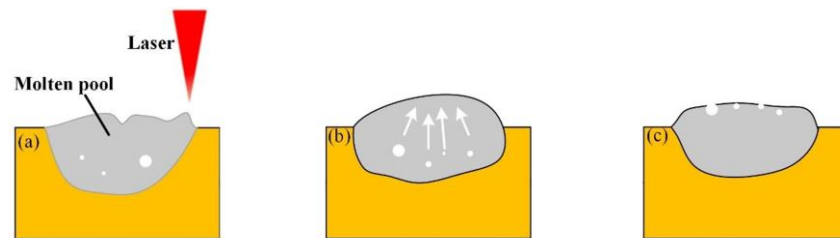


Figure 12. Diagram of the gas overflow in the molten pool during laser cladding. (a) lower preheating temperature; (b) higher preheating temperature; (c) the highest preheating temperature.

When the preheating temperature was 400 °C, there were some cracks at the bottom of the cladding coating, as shown in Figure 13. Higher preheating temperatures increase the heat accumulation in the molten pool, which brings larger thermal stress and shrinkage between the different phases. When the thermal stress is higher than the tensile strength of the cladding coating during the cooling of the molten pool, cracks may appear in some places, such as the crack in Figure 13.

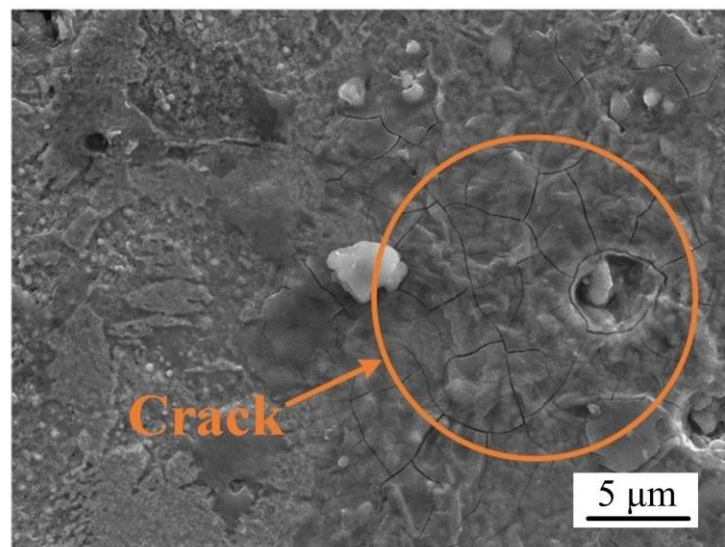


Figure 13. Crack at the bottom of the coating preheated at 400 °C.

4.2. Effect of Preheating Temperature on Microstructure

The microstructure evolution under four preheating temperatures is shown in Figure 14. When the preheating temperature is 100 °C, a large number of equiaxed crystals form in the top part of cladding coating, which do not grow due to the lower preheating temperature. With the decrease in preheating temperature, the crystals begin to grow as dendrite crystals in the middle of the cladding coating. When the preheating temperature is 200 °C, because of the increase in preheating temperature, the higher temperature promotes crystals to grow as fine cellular crystals in the top of the coating. When the preheating temperatures are 300 and 400 °C, although the microstructure of top regions is also cellular, the number

of cellular crystals is more than that of the coating preheating at 200 °C. Because of the larger cooling rate and mutual inhibition, the cellular crystals are smaller. In the middle regions, a large amount of heat accumulates in the molten pool and the secondary dendrites grow on the basis of the primary dendrites. However, when the preheating temperature is 400 °C, the higher preheating temperature causes more substrate elements into the liquid molten pool and appear in the $\text{Cu}_{0.64}\text{Zn}_{0.36}$ phase, which destroys the growth of the primary dendrites and secondary dendrites.

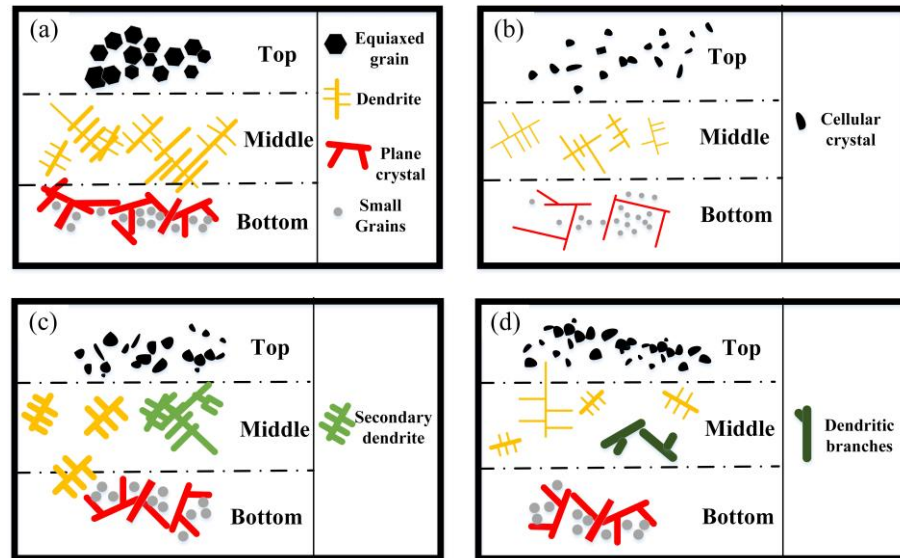


Figure 14. Microstructure evolution of four preheating temperatures. (a) 100 °C; (b) 200 °C; (c) 300 °C; (d) 400 °C.

5. Conclusions

(1) Four Ni-based alloy coatings with different preheating temperatures were successfully fabricated on the copper substrate. When the preheating temperature is 100 °C, there are some pores at the bottom of coating. When the preheating temperature is 400 °C, the effect of thermal stress is too great and a few cracks appear. At the four different preheating temperatures, the dilution rates were 27%, 20%, 29% and 40%, respectively. The coating with a preheating temperature of 200 °C has the lowest dilution rate (20%), which can maintain the property of the coating and reduces the mix of elements between the substrate and coating.

(2) When the preheating temperature is 100 °C, the main phases are γ (Fe, Ni), WC, W_2C , Ni_3B and M_7C_3 (M=Fe, Cr). When the preheating temperature is 200 °C, a new phase $\text{Cr}_{0.09}\text{Fe}_{0.7}\text{Ni}_{0.21}$ appears. When the preheating temperatures are 300 and 400 °C, a large number of substrate elements enter into the coating and form $\text{Cu}_{0.64}\text{Zn}_{0.36}$ and $\text{Ni}_2\text{W}_4\text{C}$ phases. The microstructure of the cladding coating is mainly composed of cellular, dendrite and planar crystals. The coating preheated at 200 °C has fine and uniform crystals.

(3) At the four different preheating temperatures, the values of average microhardness for the four coatings are 614.3, 941.6, 668.1 and 663.1 $\text{HV}_{0.5}$, respectively. When the preheating temperature is 200 °C, it has the maximum average microhardness, which is caused by the reinforced phases M_7C_3 , WC, Ni_3B and $\text{Cr}_{0.09}\text{Fe}_{0.7}\text{Ni}_{0.21}$ and the fine crystals in the top region. However, when the preheating temperature is 300 °C, some new phases ($\text{Cu}_{0.64}\text{Zn}_{0.36}$ and $\text{Ni}_2\text{W}_4\text{C}$) appear due to the entrance of Cu and Zn elements from the copper substrate, which decreases the coating's microhardness.

(4) The friction coefficients of the four coatings are about 0.2, 0.1, 0.2 and 0.3, respectively. The coating with a preheating temperature of 200 °C has the smallest friction coefficient (around 0.1), which also has a small fluctuation, whereas the coating with a preheating temperature of 400 °C has the largest friction coefficient (around 0.3) and fluctu-

ation. The wear rates of the coatings preheated at 100, 200, 300 and 400 °C are 9.7, 4.9, 12.5 and $13.3 \times 10^{-5} \text{ mm}^3 \cdot \text{N}^{-1} \cdot \text{m}^{-1}$, respectively. The wear rate of the coating preheated at 200 °C is the lowest due to the existence of the reinforced phases and fine crystals.

(5) When the preheating temperature is 100, 200, 300 and 400 °C, the corrosion potentials are -0.708 , -0.690 , -0.893 and -0.817 V, respectively. Moreover, the minimum values for the corrosion current density are 3.26×10^{-5} , 2.34×10^{-7} , 4.02×10^{-6} and $4.21 \times 10^{-6} \text{ mA} \cdot \text{mm}^{-2}$, respectively. The coating with a preheating temperature of 200 °C has the maximum corrosion potential (-0.69 V) and the lowest corrosion current density ($2.34 \times 10^{-7} \text{ mA} \cdot \text{mm}^{-2}$), which represents the best corrosion resistance. This is due to the high amount of Cr7C3 in the coating with a preheating temperature of 200 °C and the diffusion of a smaller amount of Cu and Zn elements into the coating.

Author Contributions: Software, Y.L.; Writing—original draft, T.X. and H.J.; Resources, Y.L.; Data processing, Y.G. and F.D.; Investigation, Z.X., D.Z. and Y.G.; Formal analysis, M.Y. and D.Z.; Supervision, Y.L., Y.G. and M.Y. All authors have read and agreed to the published version of the manuscript.

Funding: This research was funded by the Science and Technology Development of Jilin Province, grant number 20230101335Jc. This thesis work is also supported by Northeast Electric Power University.

Data Availability Statement: Data are contained within the article.

Conflicts of Interest: Author Z.X. was employed by the company Beijing Electric Power Transmission and Transformation Company Limited. The remaining authors declare that the research was conducted in the absence of any commercial or financial relationships that could be construed as a potential conflict of interest.

References

1. Wang, Y.L.; Zhuo, L.C.; Yin, E.H. Challenges and potentials/trends of tungsten-copper (WCu) composites/pseudo-alloys: Fabrication, regulation and application. *Int. J. Refract. Met. H* **2021**, *100*, 105648. [\[CrossRef\]](#)
2. Ebrahimi, M.; Par, M. Twenty-year uninterrupted endeavor of friction stir processing by focusing on copper and its alloys. *J. Alloys Compd.* **2019**, *781*, 1074–1090. [\[CrossRef\]](#)
3. Zhang, H.; Fu, H.; Zhu, S.; Yong, W.; Xie, J. Machine learning assisted composition effective design for precipitation strengthened copper alloys. *Acta Mater.* **2021**, *215*, 117118. [\[CrossRef\]](#)
4. Rao, T.S.; Bera, S. Protective layer dissolution by chlorine and corrosion of aluminum brass condenser tubes of a nuclear power plant. *Eng. Fail. Anal.* **2021**, *123*, 105307.
5. Zhou, H.-H.; Liao, Z.-W.; Fang, C.-X.; Li, H.-X.; Feng, B.; Xu, S.; Cao, G.-F.; Kuang, Y.-F. Pulse electroplating of Ni-W-P coating and its anti-corrosion performance. *Trans. Nonferrous Met. Soc. China* **2018**, *28*, 88–95. [\[CrossRef\]](#)
6. Li, T.; Dang, N.; Liang, M.; Guo, C.; Lu, H.; Ma, J.; Liang, W. TEM observation of general growth behavior for silver electroplating on copper rod. *Appl. Surf. Sci.* **2018**, *451*, 148–154. [\[CrossRef\]](#)
7. Zang, J.; Li, H.; Sun, J.; Shen, Y.; Su, N.; Feng, X. Microstructure and thermal conductivity of Cu-Cu2AlNiZnAg/diamond coatings on pure copper substrate via high-energy mechanical alloying method. *Surf. Interfaces* **2020**, *21*, 100742. [\[CrossRef\]](#)
8. Liu, Y.; Xu, T.; Liu, Y.; Gao, Y.; Di, C. Wear and heat shock resistance of Ni-WC coating on mould copper plate fabricated by laser. *J. Mater. Res. Technol.* **2020**, *9*, 8283–8288. [\[CrossRef\]](#)
9. Sciacca, G.; Sinico, M.; Cogo, G.; Bigolaro, D.; Pepato, A.; Esposito, J. Experimental and numerical characterization of pure copper heat sinks produced by laser powder bed fusion. *Mater. Des.* **2022**, *214*, 110415. [\[CrossRef\]](#)
10. Guan, W.; Gao, M.; Lv, H.; Yuan, J.; Chen, D.; Zhu, T.; Fang, Y.; Liu, J.; Wang, H.; Tang, Z.; et al. Laser cladding of layered Zr/Cu composite cathode with excellent arc discharge homogeneity. *Surf. Coatings Technol.* **2021**, *421*, 127454. [\[CrossRef\]](#)
11. Liu, Y.; Li, Z.Y.; Li, G.H.; Tang, L. Friction and wear behavior of Ni-based alloy coatings with different amount of WC-TiC ceramic particles. *J. Mater. Sci.* **2023**, *58*, 1116–1126. [\[CrossRef\]](#)
12. Feng, X.; Cui, X.; Zheng, W.; Lu, B.; Dong, M.; Wen, X.; Zhao, Y.; Jin, G. Effect of the protective materials and water on the repairing quality of nickel aluminum bronze during underwater wet laser repairing. *Opt. Laser Technol.* **2019**, *114*, 140–145. [\[CrossRef\]](#)
13. Harooni, A.; Irvani, M.; Khajepour, A.; King, J.M.; Khalifa, A.; Gerlich, A.P. Mechanical properties and microstructures in zirconium deposited by injected powder laser additive manufacturing. *Addit. Manuf.* **2018**, *22*, 537–547. [\[CrossRef\]](#)
14. Ramakrishnan, A.; Dinda, G. Microstructural control of an Al-W aluminum matrix composite during direct laser metal deposition. *J. Alloys Compd.* **2020**, *813*, 152208. [\[CrossRef\]](#)
15. Zhang, H.; Wang, L.; Zhang, S.; Wu, C.; Zhang, C.; Sun, X.; Chen, J. An investigation on wear and cavitation erosion-corrosion characteristics of the TiC modified Fe-based composite coating via laser cladding. *J. Mater. Res. Technol.* **2023**, *26*, 8440–8455. [\[CrossRef\]](#)

16. Wang, H.; Sun, Y.; Qiao, Y.; Du, X. Effect of Ni-coated WC reinforced particles on microstructure and mechanical properties of laser cladding Fe-Co duplex coating. *Opt. Laser Technol.* **2021**, *142*, 107209. [[CrossRef](#)]
17. He, B.-M.; Liu, X.-B.; Zhang, F.-Z.; Liu, Z.-Y.; Zhang, S.-H. Tribological and oxidation behaviors of TiN reinforced Co matrix composite coatings on Inconel718 alloy by laser cladding. *Tribol. Int.* **2023**, *188*, 108781. [[CrossRef](#)]
18. Liu, Y.; Wu, Y.; Ma, Y.; Gao, W.; Yang, G.; Fu, H.; Xi, N.; Chen, H. High temperature wear performance of laser cladding Co06 coating on high-speed train brake disc. *Appl. Surf. Sci.* **2019**, *481*, 761–766. [[CrossRef](#)]
19. Naizabekov, A.; Samodurova, M.; Bodrov, E.; Lezhnev, S.; Samoilova, O.; Trofimov, E.; Mikhailov, D.; Litvinyuk, K.; Trofimova, S.; Latfulina, Y.; et al. Use of laser cladding for the synthesis of coatings from high-entropy alloys reinforced with ceramic particles. *Case Stud. Constr. Mater.* **2023**, *19*, e02541. [[CrossRef](#)]
20. Wu, T.; Yu, L.T.; Chen, G.; Wang, R.Q.; Xue, Y.P.; Lu, Y.H.; Luan, B.L. Effects of Mo and Nb on the microstructure and high temperature oxidation behaviors of CoCrFeNi-based high entropy alloys. *J. Mater. Res. Technol.* **2023**, *27*, 1537–1549. [[CrossRef](#)]
21. Zhu, L.; Xue, P.; Lan, Q.; Meng, G.; Ren, Y.; Yang, Z.; Xu, P.; Liu, Z. Recent research and development status of laser cladding: A review. *Opt. Laser Technol.* **2021**, *138*, 106915. [[CrossRef](#)]
22. Bysakh, S.; Chat, K.; Maiwald, T. Microstructure evolution in laser alloyed layer of Cu-Fe-Al-Si on Cu substrate. *Mater. Sci. Eng. A* **2004**, *375*, 661–665. [[CrossRef](#)]
23. Li, Y.M.; Song, J.G.; Wang, L. Structure and Wear Performance of Laser Cladding Ni-Based Coatings on Aluminum Bronze Surface. *Mater. Prot.* **2012**, *45*, 30–32+2.
24. Su, Z.; Li, J.; Shi, Y.; Ren, S.; Zhang, Z.; Wang, X. Effect of process parameters on microstructure and tribological properties of Ni60A/Cr₃C₂ laser cladding on 60Si₂Mn steel. *Surf. Coatings Technol.* **2023**, *473*, 130005. [[CrossRef](#)]
25. Kumar, V.; Kumar, R.; Das, A.K. Comprehensive study of process parameters and their effect on tribological properties of laser clad Ti6Al4V alloy: A review. *Mater. Today Proc.* **2023**, *23*, 2214–7853. [[CrossRef](#)]
26. Chen, T.; Wu, W.; Li, W.; Liu, D. Laser cladding of nanoparticle TiC ceramic powder: Effects of process parameters on the quality characteristics of the coatings and its prediction model. *Opt. Laser Technol.* **2019**, *116*, 345–355. [[CrossRef](#)]
27. Liu, Y.; Xu, T.; Li, G.; Li, Z.; Du, F.; Chen, G. A multi-objective optimization of laser cladding process of Ni-based coating on the preheated copper alloy. *Mater. Today Commun.* **2023**, *35*, 105614. [[CrossRef](#)]
28. Lai, Q.; Abrahams, R.; Yan, W.Y.; Qiu, C.; Mutton, P.; Paradowska, A.; Fang, X.Y.; Soodi, M.; Wu, X.H. Effects of preheating and carbon dilution on material characteristics of laser-clad hypereutectoid rail steels. *Mater. Sci. Eng. A* **2018**, *712*, 548–563. [[CrossRef](#)]
29. Bidron, G.; Doghri, A.; Malot, T.; Fournier-Dit-Chabert, F.; Thomas, M.; Peyre, P. Reduction of the hot cracking sensitivity of CM-247LC superalloy processed by laser cladding using induction preheating. *J. Am. Acad. Dermatol.* **2020**, *277*, 116461. [[CrossRef](#)]
30. Weisheit, A.; Rittinghaus, S.-K.; Dutta, A.; Majumdar, J.D. Studies on the effect of composition and pre-heating on microstructure and mechanical properties of direct laser clad titanium aluminide. *Opt. Lasers Eng.* **2020**, *131*, 106041. [[CrossRef](#)]
31. Zhou, L.; Chen, S.; Wei, M.; Liang, J.; Liu, C.; Wang, M. Microstructure and properties of 24CrNiMoY alloy steel prepared by direct laser deposited under different preheating temperatures. *Mater. Charact.* **2019**, *158*, 109931. [[CrossRef](#)]
32. Hastie, J.C.; Koelblin, J.; Kartal, M.E.; Attallah, M.M.; Martinez, R. Evolution of internal pores within AlSi10Mg manufactured by laser powder bed fusion under tension: As-built and heat treated conditions. *Mater. Des.* **2021**, *204*, 109645. [[CrossRef](#)]

Disclaimer/Publisher's Note: The statements, opinions and data contained in all publications are solely those of the individual author(s) and contributor(s) and not of MDPI and/or the editor(s). MDPI and/or the editor(s) disclaim responsibility for any injury to people or property resulting from any ideas, methods, instructions or products referred to in the content.